Biomed Microdevices (2008) 10:823–837
DOI 10.1007/s10544-008-9197-0

A micro-tactile sensor for *in situ* tissue characterization in minimally invasive surgery

M. A. Qasaimeh · S. Sokhanvar · J. Dargahi · M. Kahrizi

Published online: 24 June 2008

Abstract This study presents and characterizes a micro-tactile sensor that can be integrated within MIS graspers. The sensor is capable of measuring contact forces and characterizing softness. The grasping forces are distributed normally, though in some cases concentrated loads also appear at the contact surfaces. In the latter case, the position of the concentric load can also be determined. This enables the sensor to detect hidden anatomical features such as embedded lumps or arteries. The microfabricated piezoelectric-based sensor was modeled both analytically and numerically. In a parametric study the influence of parameters such as length, width, and thickness of the sensor was studied using a finite element model. The sensor was microfabricated and tested using elastomeric samples. There is a good conformity between the experimental and theoretical results.

Keywords Micro-tactile sensor · Tissue characterization · Endoscopic graspers · Minimally Invasive Surgery (MIS)

M. A. Qasaimeh (✉) · S. Sokhanvar · J. Dargahi
Tactile Sensing and Medical Robotics Laboratory,
Department of Mechanical and Industrial Engineering,
Concordia University,
1455 De Maisonneuve Blvd. West,
Montreal, QC H3G 1M8, Canada
e-mail: mohammad.qasaimeh@mail.mcgill.ca

M. A. Qasaimeh · M. Kahrizi
MEMS and NanoDevices Laboratory,
Department of Electrical and Computer Engineering,
Concordia University,
1455 De Maisonneuve Blvd. West,
Montreal, QC H3G 1M8, Canada

1 Introduction

Useful information is supplied by the sensory interactions between humans and the surrounding environment during different manual tasks. Thanks to subcutaneous mechanoreceptor cells, our sense of touch is capable of determining the shape, size, softness and temperature of objects. By using our sense of touch, we can perform many precise and delicate tasks with our hands. Were we deprived of this feeling, the story would be complicated. Our ability would be limited and we would have poor tactile precision (Dargahi and Najarian 2004). Recently, many researchers have begun investigating tactile sensing in a variety of applications including manipulators, virtual reality, and especially medical treatment (Howe et al. 1995). In the medical field, minimally invasive surgery (MIS) has been the focus of much of the attention. MIS procedures have been widely accepted because of their many benefits. Many research centers and companies have focused on the development of MIS as a replacement for many types of traditional open surgeries. Despite the many advantages of MIS, the lack of the sense of touch has created a serious challenge for surgeons and has reduced the safety and efficiency of surgical operations. That is because soft tissue can be properly inspected and assessed by evaluating its softness, viscosity, and elasticity properties (Melzer et al. 1994; Rebello 2004). One of the very important evaluation procedures during surgery is the palpation of tissues and organs. It is an essential step for any surgical process (Howe et al. 1995; Howe and Matsuoka 1999; Webster 1988; Ottermo et al. 2004; Peine et al. 1994; Nahas et al. 2002; Kurodaa et al. 2005).

During open surgeries, a surgeon can palpate tissues to examine the size, consistency, texture, location, and tenderness of an organ. However, this tactile information

is not available in MIS operations since the current associated tools are incapable of providing any kind of tactile feedback. Although visual feedback has provided surgeons with some information that has promoted the quality of endoscopic surgery to its present level, restoring the lost tactile information could play an important role in the advancement of MIS to the next level of sophistication.

When the material specifications of an object are required, the general procedure is to prepare a sample using standard procedures. Although this method is very common and efficient in many industrial applications, it has serious shortcomings when dealing with soft tissue. The properties of soft tissue vary considerably when they are separated from the body. This can be attributed to at least two main factors: first, maintaining water content, temperature, and nutrition of tissue outside the body (i.e., *ex vivo*) is difficult, and hence the testing condition can be essentially different from that of the *in vivo* condition. Second, soft tissues in the body are normally under tension. Therefore, the initial and boundary conditions of tissue in *in vivo* and *in situ* conditions can differ from the laboratory testing condition (Brown et al. 2003). Therefore, the development of a smart grasper for the measurement of tissue properties in *in vivo* and *in situ* conditions will be highly useful.

The application of micro-electro-mechanical-systems (MEMS) technology in the fields of tactile sensing and medical tools has been widely accepted because MEMS offers flexibility, miniaturization capability, and low production costs due to batch microfabrication (Melzer et al. 1994; Rebello 2004). Several types of tactile sensors that are able to provide some of the desired information have been proposed for MIS procedures (Howe et al. 1995; Melzer et al. 1994; Ottermo et al. 2004; Peine et al. 1994; Qasaimeh et al. 2006; Dargahi et al. 2007a; Dargahi et al. 2007b). For instance, a micromachined sensor for an endoscopic grasper was presented by Dargahi et al. (2000). The sensor showed good linearity and a high dynamic response; however, it was unable to provide an adequate indication of the softness of grasped tissues. Another study (Narayanan et al. 2006; Dargahi et al. 2007c) described a piezoelectric polyvinylidene fluoride (PVDF) based tactile sensor for MIS applications. Although this sensor is capable of measuring tissue properties, it cannot be considered as a good candidate for batch manufacturing and commercial use because of its complex structure. Moreover, the sensor is active only at the teeth regions. The other regions are null and unable to detect contacting forces and properties. Recently, Sokhanvar et al. have introduced a sensor for tissue softness characterization in MIS (Sokhanvar et al. 2007a). The sensor is able to differentiate the softness of grasped objects. However, the sensor is active only at the teeth shapes; the other regions are insensitive and cannot detect any tactile property. In an alternative design, a membrane-based tactile sensor for MIS applications was presented (Golpaygani et al. 2007; 2008; Emamieh et al. 2008). The proposed sensor is active on the mesa points (projections). The other areas are not capable of providing tactile information about the grasped object. In addition, the presented sensor does not have a teeth shape and is unable to grip soft slippery tissues. In another study, a silicon tactile imager based on an array of capacitive cells was developed by Suzuki et al. (1990). The piezoresistive and capacitive pressure sensors were also studied (Samaun and Angell 1973; Lee and Wise 1982; Tanigawa et al. 1985). To sum up, a review of these studies shows that the proposed tactile sensors are mainly limited to force sensing, and they are thus unable to characterize grasped tissues. Some of the disclosed tactile sensors that are able to measure tissue properties suffer from structural complexity and are difficult to microfabricate using conventional miniaturization techniques such as MEMS.

The present study introduces a new MEMS tactile sensor for tissue softness characterization in MIS procedures. Piezoelectric polyvinylidene fluoride (PVDF) was chosen as the sensing element because of its advantages (Qasaimeh et al. 2006; Dargahi et al. 2000; Narayana et al. 2006; Sokhanvar et al. 2007b). The sensor is designed such that it can be easily batch-produced using MEMS techniques. Consistent with the existing MIS graspers, it is corrugated and suitable for grasping slippery tissues. Furthermore, it is the entire surface area of the sensor that is able to detect and report the tactile information gathered. The novel design of the sensor gives the sensor the capability of measuring grasping forces, of locating the force position as well as of estimating contact object softness. The ability to find the force position is especially important in detecting the presence of blood vessels and in locating embedded lumps inside grasped tissue.

2 The structure of the microfabricated tactile sensor

The sensor structure, which is introduced in a previous work (Qasaimeh et al. 2007), comprises three layers. The first layer with tooth-like projections is micromachined from a silicon wafer. The second layer is a patterned PVDF film working as a transducer. These two layers are supported by a third layer of Plexiglas. The first layer, which was microfabricated to form the required teeth shapes, is 100 μm thick with 200 μm high teeth-like projections on the top and two supports of 200 μm height at the bottom. The designed teeth on the top ensure a firm grasping capability. The middle part of the silicon plate would deform under a grasping action whereas the supports provide the suitable gap that is necessary for the plate

deflection. The middle part of the piezoelectric PVDF film was adhered to the middle of the silicon plate. Two other ends of PVDF film were sandwiched between the silicon supports and the Plexiglas layer. In the fabricated sensor a 25 μm-thick metalized and poled piezoelectric PVDF was used. The sensor structure is shown in Fig. 1. A set of two sensing elements at the opposite supports plus a middle sensing element form a *sensing unit*. The geometry of the grasper (e.g., the length) and the application determine the number of sensing units that are required to cover the whole length of the grasper.

The thickness of the silicon layer was chosen to be 100 μm in order to be sensitive enough to detect small mechanical forces such as the pulse of blood vessels yet robust enough to withstand the grasping loads. Different configurations of tooth-like shapes were studied and finally a checkered pattern was chosen because of its advantages (Qasaimeh et al. 2007). Figure 2(a) shows the teeth-shapes of a commercial endoscopic grasper. Figure 2(b) shows the corrugated shape of the proposed sensor as well as its integration into an endoscopic grasper.

The silicon layer was etched from both sides to form the teeth-shapes on the top and the U-channel on the bottom using TMAH anisotropic bulk etching. To protect the teeth corners, a convex corner compensation technique was used. To form three sensing units, the PVDF film was also

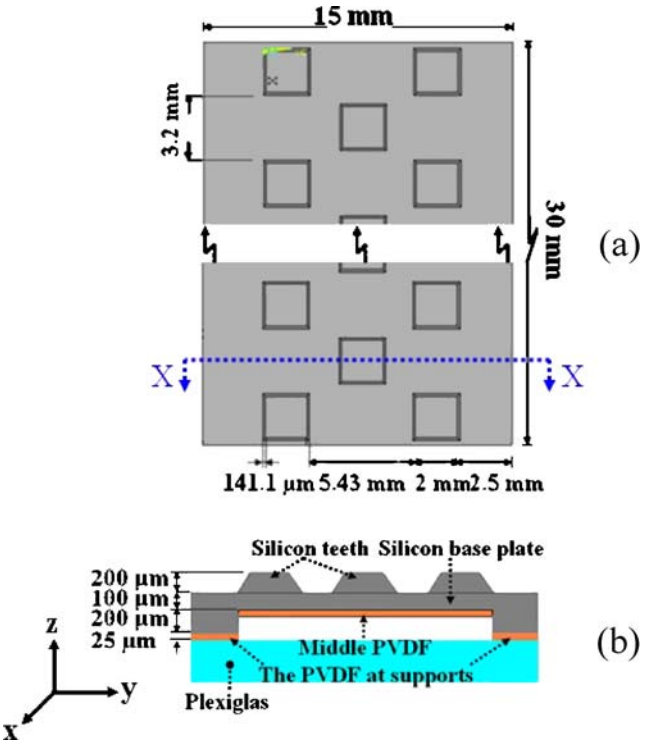

Fig. 1 Structure of the sensor. (**a**) top view of the sensor showing the major dimensions, and (**b**) the cross-section of the sensor showing the three layers and their thicknesses

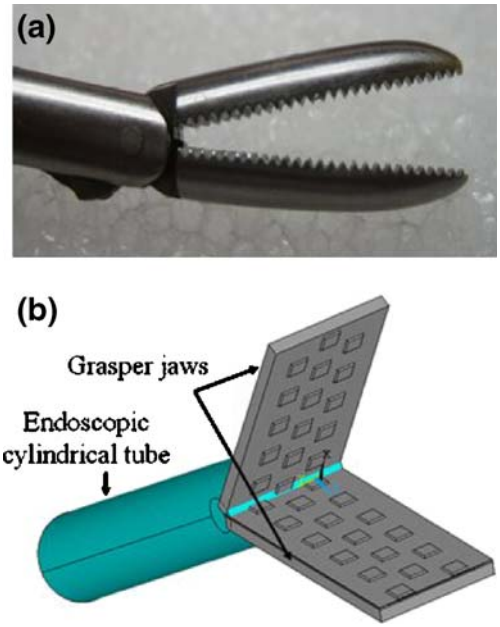

Fig. 2 Endoscopic grasper. (**a**) a typical commercial endoscopic grasper, and (**b**) how the endoscopic grasper could be equipped with the proposed sensor

patterned, using a photolithography technique. Different layers of the sensor were then assembled using nonconductive epoxy, and the electrical wires were connected to the sensing elements using silver conductive epoxy (Qasaimeh et al. 2007). The assembled sensor is shown in Fig. 3.

3 Sensor modeling: analytical approach

Before conducting a finite element analysis, a closed form formulation was used to investigate the influence of different parameters on the output of the sensing elements. Two different relationships were used: one for the sensing elements which were adhered at the supports; a second one

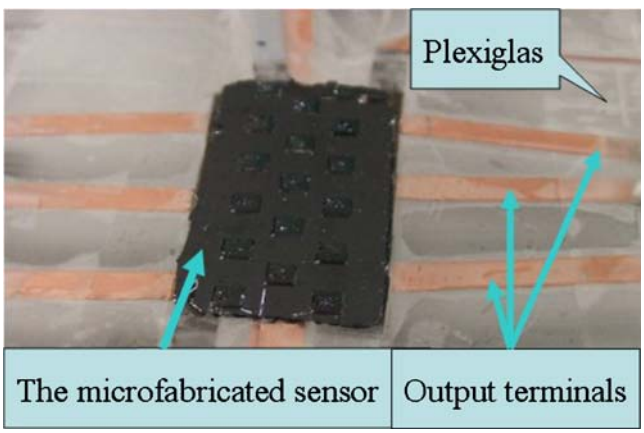

Fig. 3 The microfabricated sensor with tooth-like projections on top and electrodes to collect electrical charge

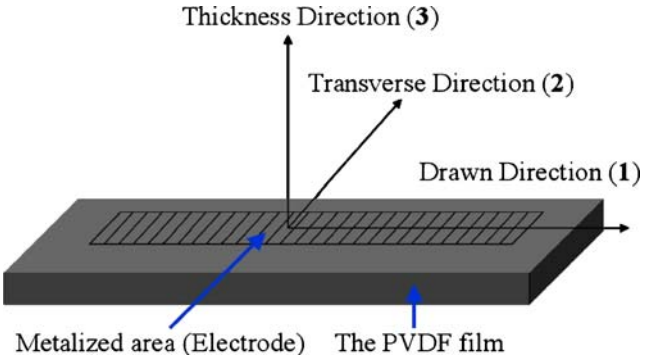

Fig. 4 The principal directions of a uniaxial PVDF film

for the sensing elements which were adhered to the middle of the silicon plate. Before deriving the formulations, a brief introduction to piezoelectric relationships is presented below.

Piezoelectric films are commercially available in two forms: uniaxial and biaxial. The uniaxial film, which was used in the present study, is the result of the mechanical drawing of the film in one direction. This direction is called the drawn direction and is referred to as the film's 1-axis and has the highest piezoelectricity coefficient. The three perpendicular preferred directions 1, 2, and 3, which are called the drawn, the transverse, and the thickness directions, respectively, are shown in Fig. 4. Since uniaxial PVDF film has three preferred directions, it is normally classified as orthotropic materials (Sokhanvar et al. 2007a).

When piezoelectric materials are strained, a charge is created. The charge is proportional to the stress and can be expressed by the following relationship (Ueberschlag 2001; Ikeda 1996; Sokhanvar et al. 2008):

$$Q_3 = \sigma_{11} d_{31} + \sigma_{22} d_{32} + \sigma_{33} d_{33} \tag{1}$$

Q_3 is the output charge collected in the third direction (i.e., the thickness); d_{31}, d_{32}, and d_{33} are the piezoelectric coefficients in the drawn, the transverse, and the thickness directions, respectively. The electrodes at the top and the bottom of the PVDF film form a capacitor, and hence the output charge can be taken as a voltage from these electrodes. The relation between the output voltage and the generated charge is given by:

$$V = Q/C \tag{2}$$

Where Q is the generated charge; C is the PVDF film's capacitance; and V is the output voltage (Ueberschlag 2001; Ikeda 1996; Sokhanvar et al. 2008).

3.1 Sensing elements at supports

When a soft object is grasped, compression forces are transmitted through the silicon layer to the PVDF films at the supports. When the grasped object is homogeneous and also there is no embedded mass, a uniform distributed load is applied to the beam and both supports carry equal loads. Therefore, an equal output charge results. However, it is possible that, in addition to the distributed load, a concentrated load would also be applied to the beam. In this case, the output voltages of the PVDF supports are in general not equal. In other words, the output voltage at each support corresponds to the part of the load that is carried by that support. Therefore, the difference between the outputs of the supports determines the location of the concentric load. By considering a fixed-fixed beam with a concentric applied load, as shown in Fig. 5, there are two reactions and two moments at the fixed points of the beam referred to as R_1, R_2, M_1, and M_2.

For a system in static equilibrium, the values of R_1 and R_2 can be found from the following relationships:

$$R_1 = \frac{P\left(\lambda^3 - 3\lambda y^2 + 2y^3\right)}{\lambda^3} \tag{3}$$

$$R_2 = \frac{P(3\lambda y^2 - 2y^3)}{\lambda^3} \tag{4}$$

where λ is the length of the beam on which load P is applied at distance y.

The PVDF sensing elements at the supports work in thickness mode. Therefore, the substitution of Eqs. 1 and 2 into 3 and 4 gives the voltage output generated at supports 1 and 2.

$$V_{R1} = \frac{Pd_{33}\left(\lambda^3 - 3\lambda y^2 + 2y^3\right)}{C\lambda^3} \tag{5}$$

$$V_{R2} = \frac{Pd_{33}(3\lambda y^2 - 2y^3)}{C\lambda^3} \tag{6}$$

By knowing the output voltages of PVDF films at the supports (i.e., V_{R1} and V_{R2}), the magnitude and location of the applied load can be obtained from the two equations above. Figure 6 shows the normalized output voltages of PVDF films at the supports when a concentric load is

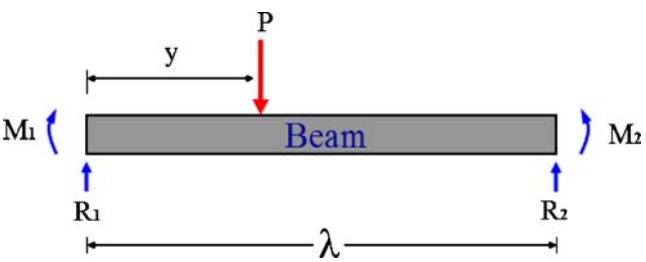

Fig. 5 A simple fixed-fixed beam with concentric load application

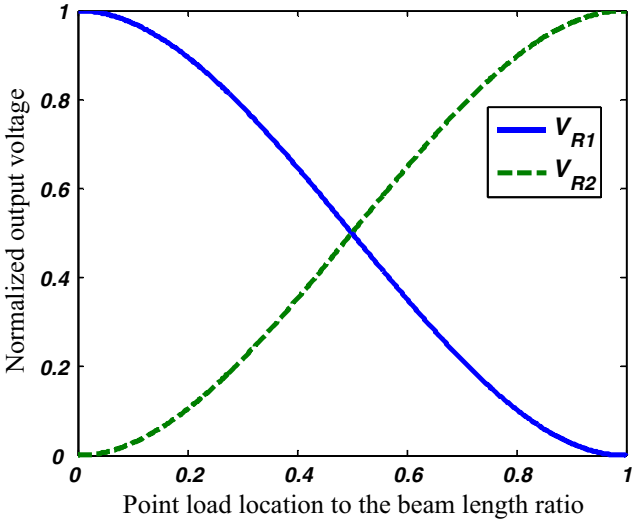

Fig. 6 Normalized output voltage of the supports sensing elements as a function of the point load location. The symbol V_{R1} denotes the output voltage from the PVDF film at support 1. Alternatively, V_{R2} is the output voltage from the PVDF film at support 2

applied at different points along the length of the beam. The output voltage at each PVDF film is proportional to the part of the load that is carried by the sensing element. The summation of these output voltages specifies the total grasping load. In other words, the grasping force can be measured by calibrating this summation with respect to the applied compression forces.

It was shown that the presence of an embedded lump within the grasped object appears as a concentric load at the contact surface (Qasaimeh et al. 2007). Therefore, detecting the concentric load and its position can indicate the presence of any embedded lump and also can determine its precise location (Hosseini et al. 2006). Thus, any embedded lumps can be located by comparing these output voltages.

3.2 Sensing elements in the middle

In each sensing unit, the middle sensing element is a PVDF film working in extensional mode. The deflection of the silicon plate causes the adhered PVDF layer to stretch and to supply a corresponding output voltage. This sensing element essentially determines the softness of the grasped tissue and also detects any low magnitude dynamic loads such as the pulsation of blood vessels. Two factors make middle PVDF film extremely sensitive and suitable for pulse detection. First, the piezoelectric PVDF coefficient in the drawn direction, d_{31}, is higher than the coefficients in the other directions. Second, compared to the thickness direction when a similar load is applied to the PVDF film, the resultant stress in the PVDF film is extremely high because of the thinness (e.g., 25 μm) of the PVDF film.

In this design, as shown in Fig. 7, the combined flexural rigidity of the grasped object and of the silicon layer provides resistance against the loading. Therefore, the total deflection depends on the flexural rigidity of both the silicon and the object layers. Since the material property of silicon is known, the material property of the grasped object can be determined.

For a given compressive load, when the grasped object is hard, the silicon undergoes a small deflection. Accordingly, the PVDF layer also experiences a small stretch and produces a low voltage [see Fig. 7(a)]. By contrast, when the grasped object is soft, the silicon layer is highly deflected, causing a full stretch of the PVDF and thereby a high voltage [see Fig. 7(c)]. It should also be mentioned that, regardless of the softness of the grasped object, the total load is always carried by the supports, and hence the total load is determined from the outputs of the PVDF films at the supports. Therefore, each sensing unit can determine the applied force and simultaneously the deformation that is caused by the load. The softness of the grasped object can be estimated from these two data.

Non-uniform soft tissue causes un-even deflection through the silicon plate at different sections, and hence the response of the PVDF sensing units is different. Therefore, the difference between outputs of sensing units (along the sensor length) is associated with the difference between the softness of the object along the sensor length.

To drive a simple model for softness detection, a beam and the grasped tissue are considered as depicted in Fig. 8. For a given geometry and under a compressive load, depending on the flexural rigidity of the combined beam

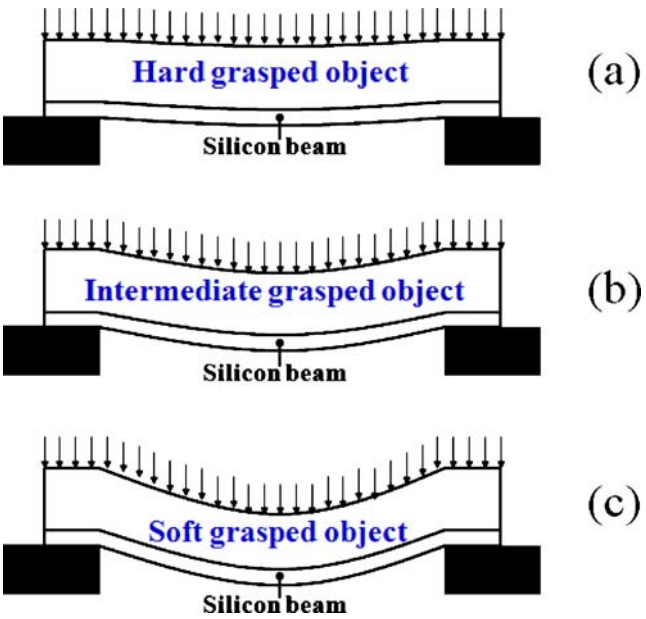

Fig. 7 The basic idea of the softness sensing: (**a**) hard grasped object, (**b**) intermediate softness of the grasped object, and (**c**) very soft grasped object

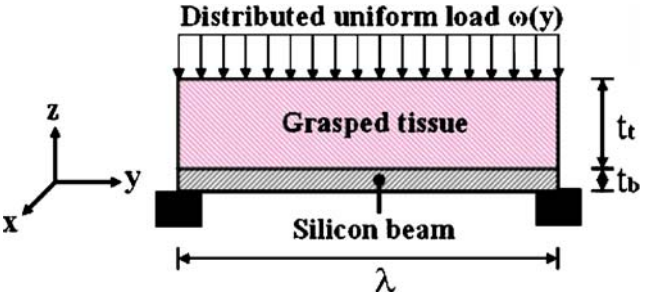

Fig. 8 A simplified model of a sensing unit. The upper jaw of the sensor is replaced with a compressive load. Subscripts *t* and *b* stand for tissue and beam, respectively

and object, the system deflects with a specific radius of curvature R. In other words, the radius R is a function of the applied load, the resultant modulus of elasticity of the system, and the resultant second moment of inertia. Since the effect of that part of the object that remains outside of the grasped region on the beam deflection is negligible, in this model it is assumed that the width of the grasped object is equal to the width of the beam.

As shown in Fig. 9, after deflection, the neutral axis (N.A.) moves to a distance c from the surface of the beam. The bending magnitude for the composite beam can be expressed as (Beer et al. c2006):

$$M_x = \left(\frac{b(c-t_t)^3 - bc^3}{3R}\right)E_t + \left(\frac{bc^3 - bt_b^3}{3R}\right)E_b \tag{7}$$

where b is the breadth of the beam, and E_t and E_b are the Young's modulus of the tissue and beam, respectively. The symbols t_t and t_b are the thickness of the tissue and beam, respectively. The first term in the bending expression is related to the tissue and the second term is related to the beam.

This composite beam can be transformed to an equivalent beam with an equivalent modulus of elasticity (E_{eq}) and an equivalent second moment of inertia (I_{eq}). Since the thickness of the grasped object is much larger than that of the beam, the thickness of the equivalent beam is considered equal to the object thickness. Therefore, the total bending (M_x) on the equivalent beam can be expressed as follows:

$$M_x = \frac{-bt_t^3}{12R}E_{eq} \tag{8}$$

By comparing the bending expression of the composite beam 7 with the bending of the equivalent beam 8, the equivalent modulus of elasticity of the composite beam can be found as the following:

$$E_{eq} = C_1E_t + C_2 \tag{9}$$

where $C_1 = \frac{4bt_b^3 - 4bc^3}{bt_t^3}$ and $C_2 = \frac{4c^3 - 4b(c-bt_t)^3}{bt_t^3}E_b$

It can be seen from the latter equation that if the modulus of elasticity of the grasped tissue (E_t) is increased, the equivalent modulus of elasticity (E_{eq}) is increased and vice-versa. The deflection profile of the equivalent beam under a distributed load $\omega(y)$ is given by (Beer et al. 2006):

$$E_{eq}I_{eq}\frac{d^4z}{dy^4} = -\omega(y) \tag{10}$$

For fixed-fixed beam boundary conditions, deflection of the equivalent beam at each point, z, reads as follows:

$$Z(y) = -\frac{\omega(y)y^2}{24E_{eq}I_{eq}}(\lambda - y)^2 \tag{11}$$

To study the influence of the modulus of elasticity of tissue on the deflection of the equivalent beam and hence the output of the middle PVDF film, consider the deflection of a specific point such as the mid-length of the beam. By substituting the equivalent modulus of elasticity and the equivalent second moment of inertia ($I_e \approx I_t$, because the object is much thicker) into the Eq. 11, the deflection of the mid-length point of the beam can be written as follows:

$$z_{mid} = \frac{C_3}{C_4E_t + C_5} \tag{12}$$

where $C_3 = -\omega(y)\lambda^4$, $C_4 = 384I_tC_1$, and $C_5 = 384I_tC_2$

As can be seen, a larger E_t results in a lower deflection. The constants C_3, C_4, and C_5 depend on the geometry and on the beam modulus of elasticity and also on the applied load. The sensor geometry is known and the applied load can be calculated from the PVDF films at the supports. Therefore, from Eq. 12 the only remaining unknown, E_t can be calculated.

The characteristics of the composite beam for typical values when the softness of the grasped object is varied are illustrated in Fig. 10.

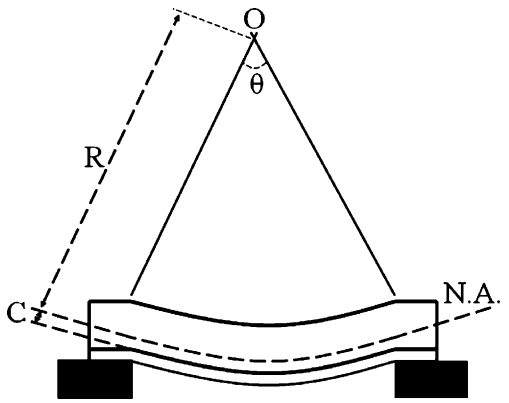

Fig. 9 Geometry of the model after deflection due to the applied compressive load

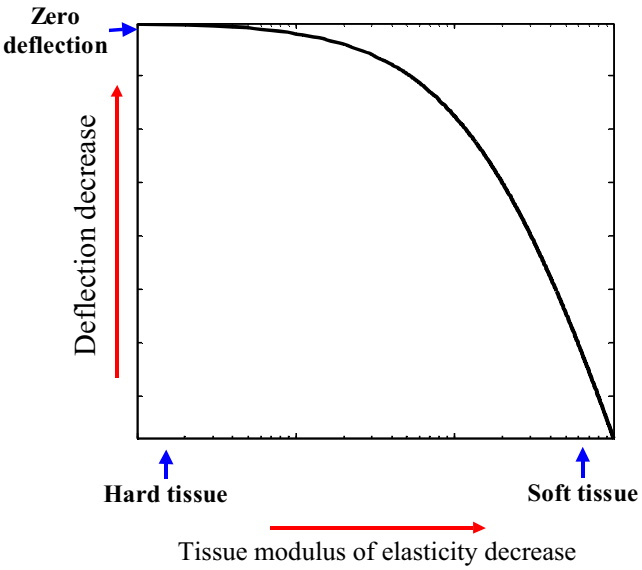

Fig. 10 Deflection of the beam versus the object softness shown in a semi-log graph

4 Sensor modeling: finite element analysis

The proposed sensor was modeled and analyzed using finite element (FE) software ANSYS Version 10. The meshed model of the sensor is shown in Fig. 11. The silicon layer was modeled using SOLID45 element, which is suitable for the three-dimensional modeling of the solid structures. It is defined by eight nodes having three degrees of freedom at each node: translations in the nodal *X*, *Y*, and *Z* directions. The SOLID227, a three-dimensional coupled-field element, was used for the modeling of both the piezoelectric PVDF layer and the structural Plexiglas layer. It has strong capabilities when dealing with problems pertinent to piezoelectricity. The SOLID227 element has ten nodes with up to five degrees of freedom per node and supports large elastic deflections. The modeled sensor has the same dimensions as the fabricated and experimentally tested sensor.

4.1 Parametrical analysis

Any change in the dimensions (e.g., length *l*, width *w*, and thickness *t*) of the designed sensor could change the characteristics, in particular the load capacity of the sensor. Therefore, using the developed finite element model a parametric study of the design was carried out. In these simulations, a 4 N point load was applied onto the center of the plate, and the stretch in the *Y*-direction with respect to different lengths, widths, and thicknesses of the sensor was calculated.

To investigate the effect of length, the other two parameters were kept constant. The width and thickness, therefore, were considered to be 15 mm and 100 μm, respectively. For a constant point load, Fig. 12 shows the relationship between the sensor length and its elongation in the *Y*-direction. It can be seen that at l=35 mm, the elongation is reduced by 38% compared to l=15 mm, when the silicon plate is a square. This reveals a remarkable dependency of the sensor output on the sensor length.

Alternatively, to study the influence of the width on the output of the sensor, the length and thickness of the plate were kept constant (30 mm for the length and 100 μm for the thickness), while the width of the plate was varied from 10 to 20 mm. The non-linear relationship between the width of the plate and its corresponding elongation is shown in Fig. 13.

Figure 14 predicts the relationship between the thickness and the resultant elongation. In these series of simulations,

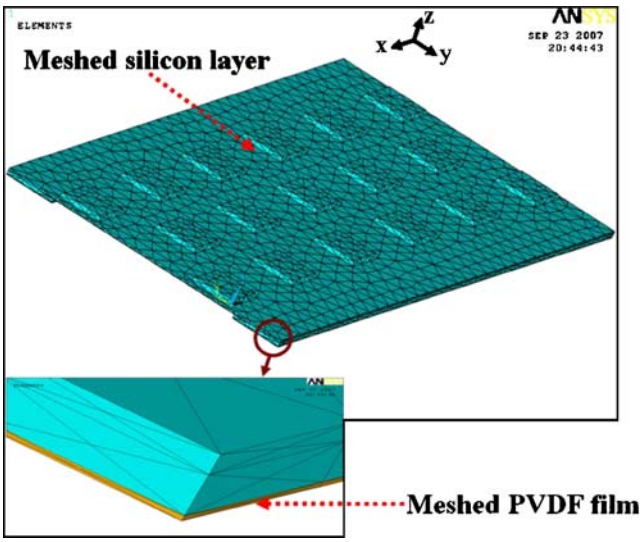

Fig. 11 Finite element meshing of the sensor

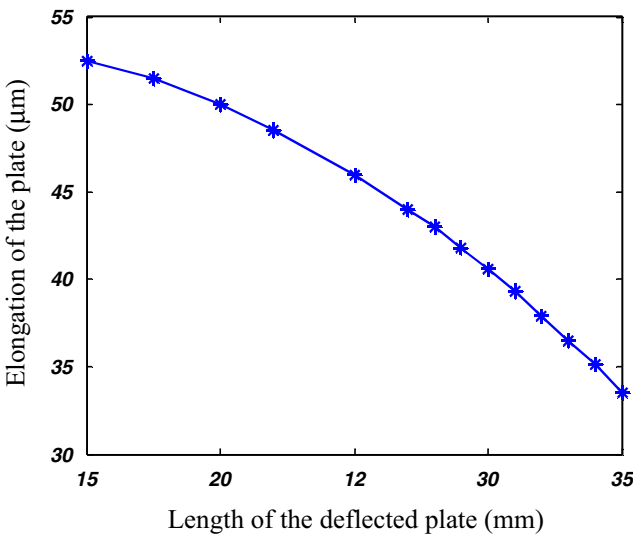

Fig. 12 The relationship between plate elongation and its length

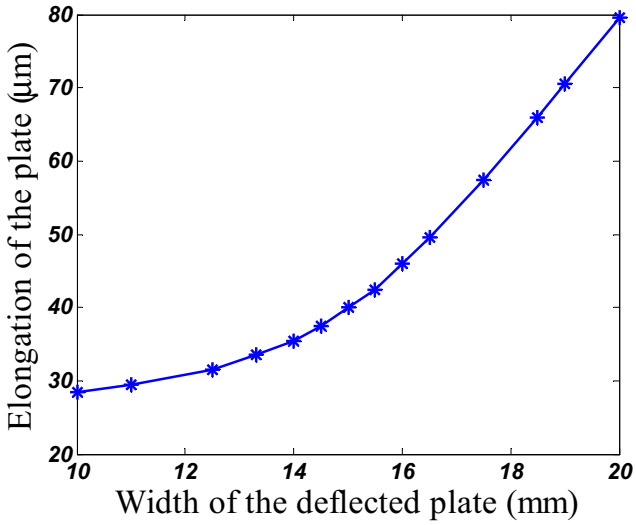

Fig. 13 Elongation of the silicon plate in *Y*-direction versus plate width

the length and the width were kept constant (30 mm for the length and 15 mm for the width) while the thickness of the plate was changed from 50 to 150 μm.

The maximum permissible point load that can be applied to the prototyped sensor (l=30 mm, w=15 mm, and t= 100 μm) was calculated to be 4 N, where the fracture strength of silicon was considered 4 GPa (Petersen 1982; Chong et al. 2003; Ericson and Schweitz 1990), and a factor of safety (F.S.=3) was taken into consideration. In that case, the elongation of the plate in the *Y*-direction was approximately 40 μm.

Since different MIS graspers have different dimensions (i.e., the length and width), the dimensions of the sensor have to be changed accordingly, to accommodate each type of endoscopic grasper. Therefore, for each new grasper size a new analysis is required to determine the optimized dimensions with respect to the load range. However, using a set of simulations, all other combinations of the thickness, length, and width with the same elongations for the maximum load (4 N) and minimum load (10 mN) were carried out. The ranges used for this analysis were the following: 10–40 mm, 7.5–20 mm, and 50–150 μm for the length, width, and thickness, respectively. A code was developed in the FE software ANSYS 10, in which each dimension was changed incrementally. Each parameter was changed within the given range (30 steps for the length, 25 steps for the width, and 20 steps for the thickness). As one parameter was changed, the other two dimensions were kept constant. The results of changing three parameters (dimensions) with the mentioned number of steps were 15,000 combinations. The code calculated the elongation of the plate for each combination. Out of these 15,000 combinations, 145 cases were found to have an elongation very close to that of the prototyped sensor. The dimensions of the plates for those cases were drawn together, where each set represents a point of three-dimensional surface shown in Fig. 15. Therefore, for each new grasper, the length and width would be measured, and then, using Fig. 15, the associated thickness would be determined.

Alternatively, by having one dimension of the sensor, which could be dictated by a medical tool, the other two dimensions can be found from Fig. 15 to have the same loading and elongation as the designed prototype sensor. Consequently, the designed sensors might have different dimensions but work with the same loading range.

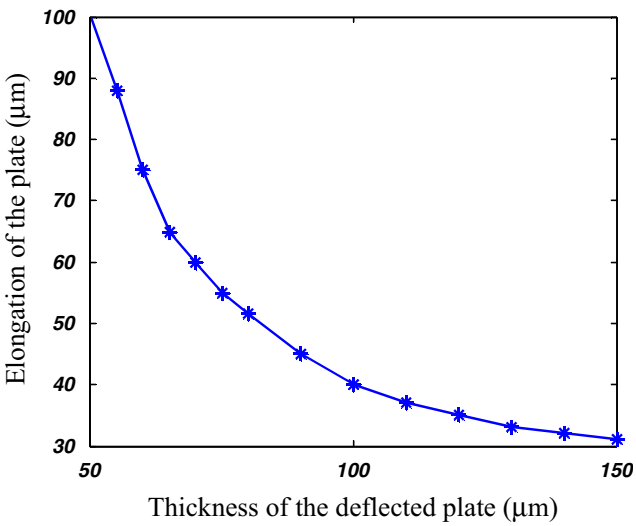

Fig. 14 The dependency of the plate elongation on its thickness

4.2 Sensing elements considerations

Since the piezoelectric PVDF film has preferred directions, as discussed earlier, the orientation of the film in the assembled structure is imperative. Therefore, to find the

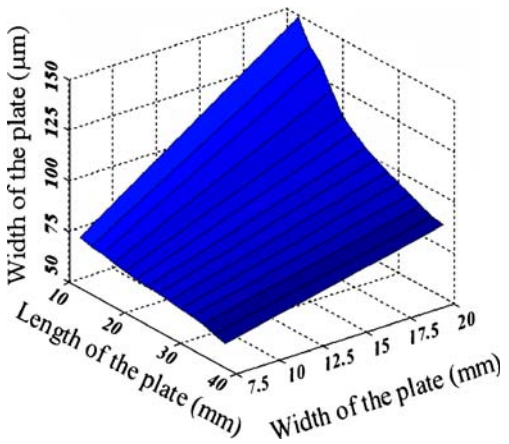

Fig. 15 All combinations of the sensor dimensions that have the same loading range. The simulations were performed on a plate with its two supports

optimal location and distribution of the PVDF sensing elements a study was carried out.

With respect to the orientation of the PVDF sensing elements, two possible cases were considered. In the first case, the drawn direction (d_{31}) of the PVDF film was oriented parallel to the sensor width (*Y*-direction). The simulation results (output voltage) for this case are shown in Fig. 16(a_1 and a_2). Figure 16(a_1) shows the voltage profile of the middle PVDF film, while Fig. 16(a_2) shows the voltage profile of the PVDF film at the supports. In the second case, the drawn direction of the PVDF layers was oriented parallel with the length of the sensor (*X*-direction). The simulation results for this case are shown in Fig. 16(b_1 and b_2). Figure 16(b_1) shows the voltage distribution in the middle PVDF film, whereas Fig. 16(a_2) shows the voltage distribution in the PVDF film at the supports. For both cases [Fig. 16(a and b)] a 1 N point load was applied on the center of the sensor.

As simulations show, when the d_{31} direction of the PVDF film was oriented parallel to the sensor width [see Fig. 16(a_1 and a_2)] higher voltage resulted. Therefore, the first case, which is shown in Fig. 16(a), was chosen for prototyping.

In order for the sensor to have the capability of finding the position of the applied load, an array of the sensing elements had to be considered. One quantity, which had to be found at this stage, was the optimized number of sensing elements and their layout on the PVDF film layer. Figure 16(a), shows that for a load which is in the desired load range, the voltage profile covers almost one third of the PVDF film (or sensor) length both in the middle and at the supports. This suggests that we should divide the PVDF film length into three longitudinal regions as shown in Fig. 17. In the present article, each PVDF film, whether it is at the middle or at a support, is called a sensing element. In addition, a set of sensing elements comprising one element at the middle and two corresponding elements at the supports is called a sensing unit. Therefore, as shown in Fig. 17, with three sensing units, there are nine sensing elements: three in the middle, three at support #1, and the remaining three covering the opposite support #2. To electrically form these nine sensing elements out of a single metalized PVDF layer, the PVDF film was patterned through etching out the aluminum coating using a mask (Qasaimeh et al. 2007). The etched out regions are also illustrated in Fig. 17.

4.3 Numerical results

The performance of the designed sensor was evaluated by simulating the physical model of the sensor using the finite element software ANSYS10. Its characteristics in lump detection and softness estimation are explained below.

4.3.1 Embedded lump detections

In order to detect the precise location of the applied point load, a point load was applied to the silicon layer at different points each time; these points are shown in Fig. 18. The output voltages of the middle sensing unit (i.e., support 12, middle 2, and support 22) with respect to the point load location, in the middle of the sensor length, and along the *Y*-direction, at different magnitudes, are shown in Fig. 19.

Alternatively, the output voltages of the sensing elements when a point load of 1 N magnitude was applied at

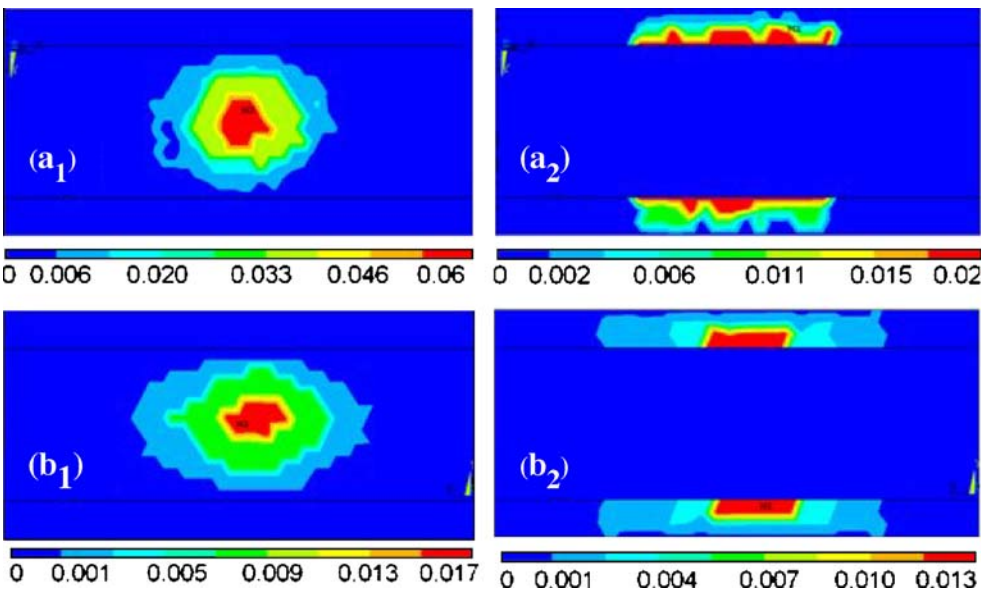

Fig. 16 Comparison of the voltage distribution of the PVDF sensing elements. First, d_{31} was oriented to the width of the sensor ($\mathbf{a}_1$, $\mathbf{a}_2$), and second, d_{31} was oriented parallel to the length of the sensor ($\mathbf{b}_1$, $\mathbf{b}_2$). The unit of the output in the legend is volt

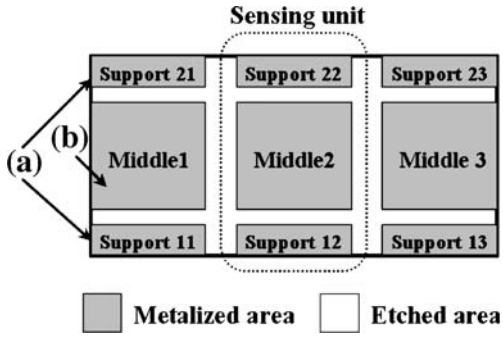

Fig. 17 Layout of the active sensing elements on the PVDF layer: (**a**) one pair of the active sensing elements at the supports, and (**b**) one of the active sensing elements in the middle. Each middle sensing element and its two associated sensing elements at the opposite supports are referred to as a sensing unit

different points along the *X*-direction and in the middle of the sensor width are shown in Fig. 20. The output from the middle sensing elements at different magnitudes is shown in Fig. 21.

As shown in Figs. 20 and 21, the magnitude of the applied point load can be detected by using the output voltage magnitude of the sensing elements. In addition, the precise location of the point load in the *XY*-plane can be detected by comparing the output voltages of the different sensing elements.

4.3.2 Softness estimations

One of the distinguishing features of this design is the capability of the sensor to measure the softness of the contacted tissues/objects. To demonstrate the performance of the sensor in softness estimation, the finite element model was modified. As shown in Fig. 22, in the augmented model, a contacting soft object/tissue and a piezoelectric PVDF layer were added.

The soft object was modeled using SOLID45 element, which also supports large deflections and large strains for three-dimensional modeling. The soft materials assumed to be homogeneous and isotropic. In addition, as discussed in Sect. 5.2, in the present work, the force and deformation

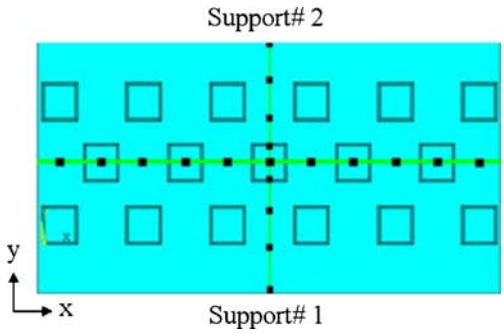

Fig. 18 Position of the applied point load along *X*- and *Y*-directions

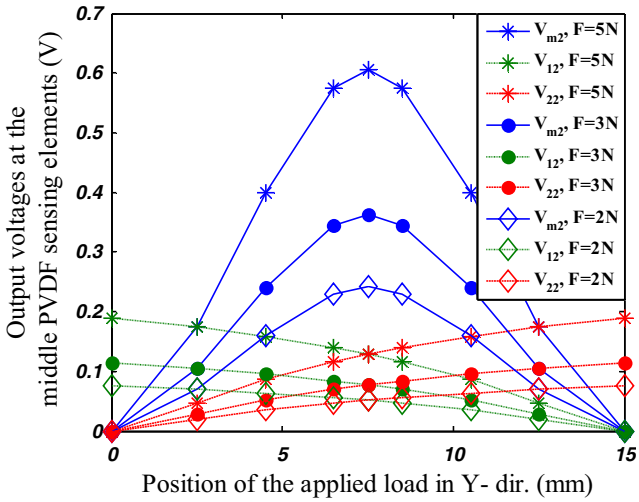

Fig. 19 Output voltages of the PVDF sensing elements when point loads with different magnitudes were applied along the *Y*-direction. The symbols V_{m2}, V_{12} and V_{22} denote the voltage of sensing elements located at middle 2, support 12, and support 22, respectively

are kept low. Therefore, the soft materials are modeled as linear elastic materials. In this case, the material property can be uniquely determined by two parameters such as Young's modulus and Poisson's ratio. For a perfectly incompressible material, the Poisson's ratio would be exactly 0.5. However, for nearly incompressible soft materials, the Poisson's ratio is less than 0.5 (Wellman and Howe 1999; Kerdok et al. 2003; Thomas et al. 2004). In the following simulations, the Poisson's ratio of the grasped object was considered to be 0.49 while its stiffness

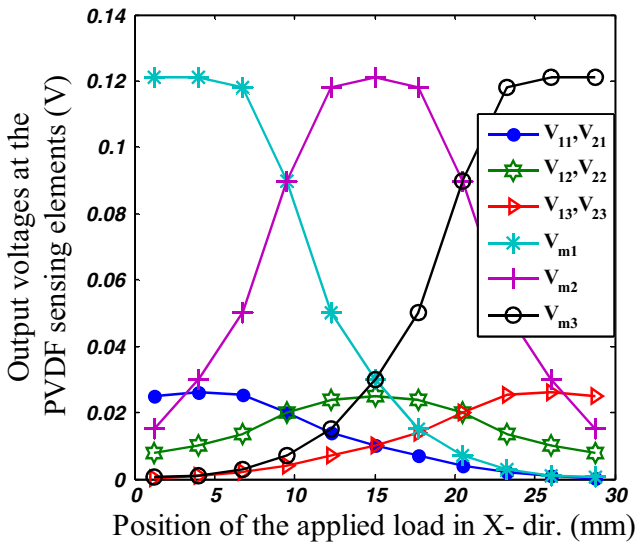

Fig. 20 Output voltages of the PVDF sensing elements when a 1 N point load is applied along the *X*-direction. The symbols V_{11} and V_{21} denote the voltage of sensing elements located at support 11, and support 21, respectively. The symbols V_{m1}, V_{m2} and V_{m3} denote the voltage of the sensing elements located at middle 1, middle 2 and middle 3, respectively

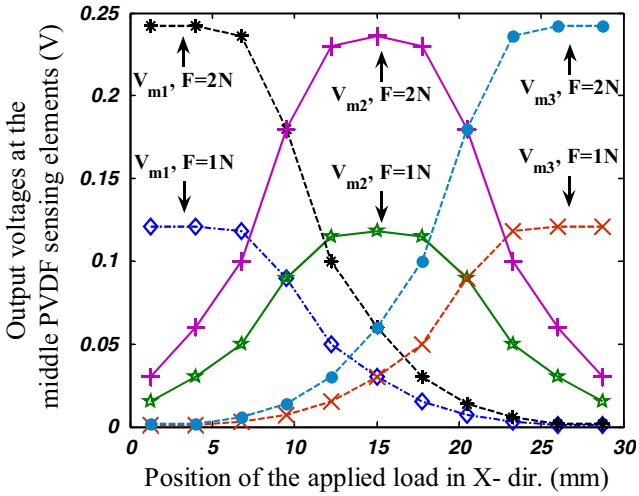

Fig. 21 Output voltages of the middle PVDF sensing elements when 1 and 2 N point loads are applied along the *X*-direction

was varied. Then the output voltages of the middle PVDF sensing elements in terms of applied forces were recorded. The uniform distributed load was applied on top of the soft object to replicate a grasping situation. Since PVDF film is adhered to the silicon layer, it experiences the same strain that the silicon plate undergoes. This strain creates charges that are collected by the aluminum electrodes as a voltage. Figure 23 shows the resulting strain on the soft object and on the silicon layer.

To characterize the sensor output in terms of softness of the grasped objects, a range of the modulus of elasticity (from 10^4 to 10^8 Pa) of the grasped object was examined. The sensor outputs when the grasping distributed load was varied from 1 to 5 N as a function of the grasped object softness are illustrated in Fig. 24. As shown in this figure, the output voltage at the middle PVDF sensing elements decreases when the grasped tissue is harder. It can also be concluded that at high grasping loads the sensitivity of the sensor increases. This is comparable to the manual palpation by a surgeon, where palpations need enough compression force to distinguish the object stiffness or any abnormality inside.

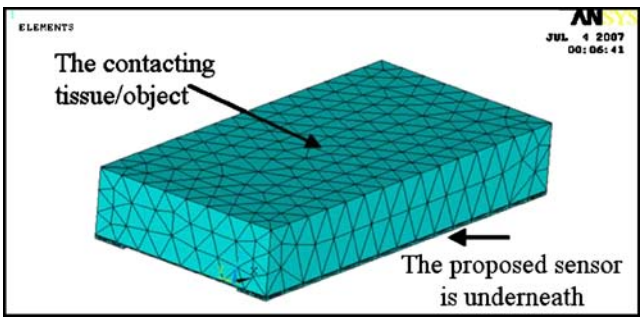

Fig. 22 The three-dimensional coupled filed finite element model of the sensor with the soft object

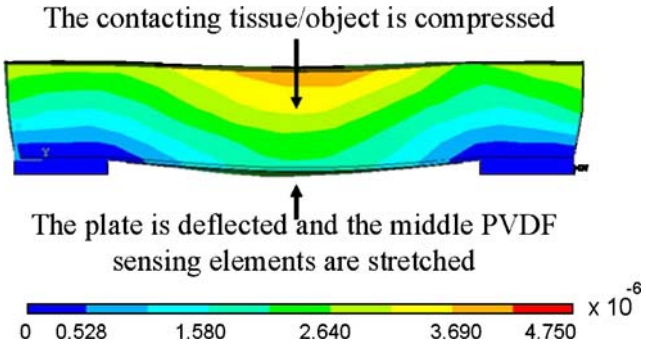

Fig. 23 A cross-sectional view of the sensor/object showing the resulting strain (dimensionless) of the sensor when a distributed load is applied on top of the object

5 Experiments

In order to amplify and register the outputs of the sensing elements, they were connected to charge amplifiers (Kistler Type 5010) and then to a computer via a data acquisition card (National Instrument, NI PCI-6225; Qasaimeh et al. 2007). The force was applied by a probe attached to a shaker. The shaker itself was driven by a power amplifier (V203, PA25E-CE, Ling Dynamic System). The amplitude and frequency of the shaker were controlled by a signal generator. A reference load cell (Kistler 9712B50) was connected to the probe to measure the actual applied force. The experimental setup is shown in Fig. 25.

5.1 Force position

A concentrated load was applied at different points in the *X* and *Y* directions at even intervals, using the experimental setup described above. The locations of the applied load are shown in Fig. 18. In the first experiment, the point load was applied along the *Y*-axis and at the middle of the length. The output voltages of the middle sensing element (V_{m2}) as well

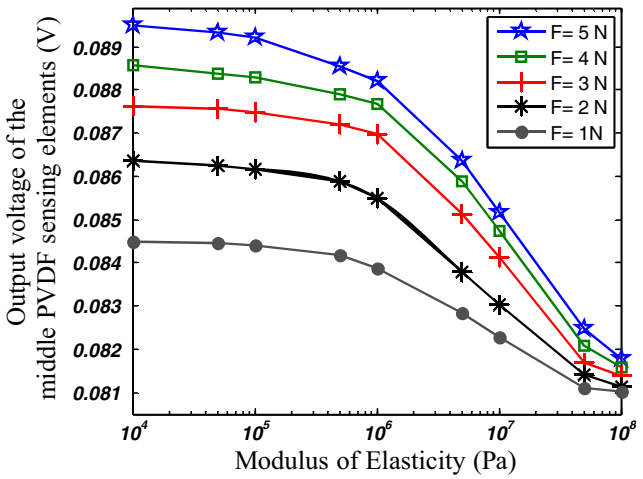

Fig. 24 Output voltages of the middle PVDF sensing elements versus different object stiffnesses at different grasping loads

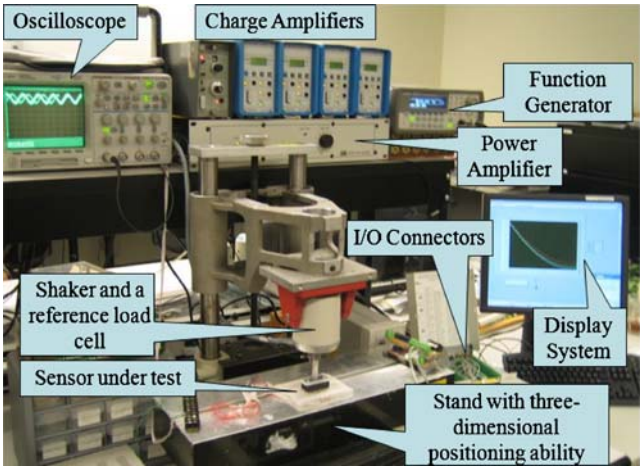

Fig. 25 Photograph of the experimental setup

as the output voltage of the supports (V_{12} and V_{22}) were then measured. Figure 26 shows the comparison of these experimental values with the simulations results.

Then the point load was applied along the *X*-axis and in the middle of the width, and the PVDF voltages were recorded. The comparison between the experimental and the simulation output voltages from the supports and the middle sensing elements are shown in Figs. 27 and 28, respectively. In Fig. 27, each point is the summation of the output voltages of the two opposite supports at each sensing unit.

From these graphs a series of calibration look up tables can be constructed from which the location of any concentric load can be determined.

The variations between theoretical and experimental results can be attributed to factors such as the error in the location of the applied load, the error due to the reading of the peak to peak magnitude of the input force, and the electrical noise.

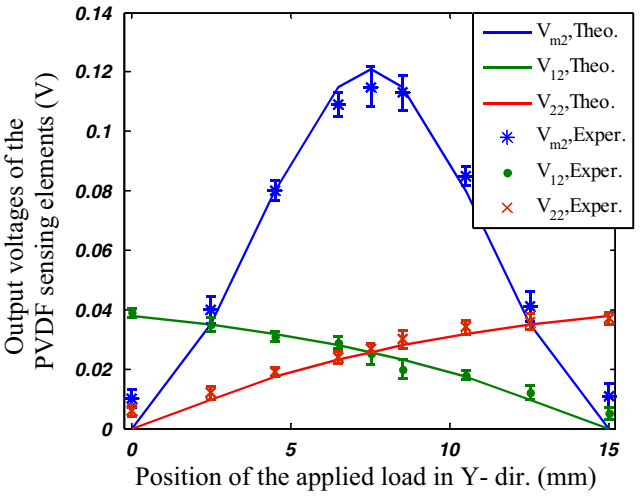

Fig. 26 Output voltages of the sensing elements when a moving concentric load is applied along the *Y*-direction, see Fig. 18. *Error bars* indicate the maximum and minimum readings

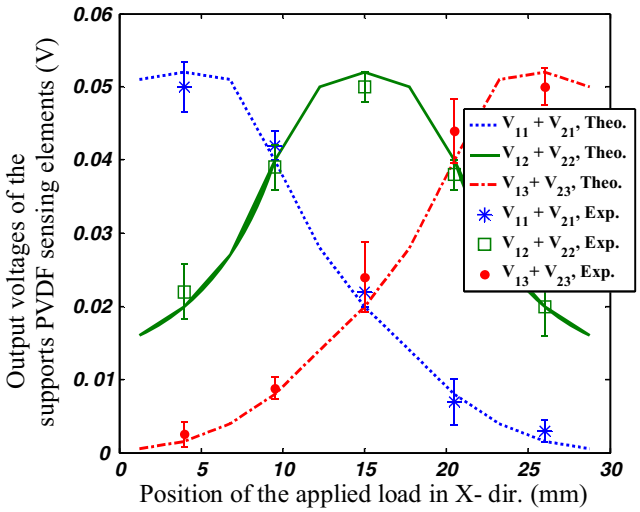

Fig. 27 Output voltages at the supports sensing elements versus the *X*-location of the load

5.2 Softness estimations

Analogous to the nature of the grasping forces in MIS graspers, a distributed load was used in softness sensing experiments. Samples of six isotropic elastomers were mechanically tested. Three rectangular prism samples were cut out of each elastomer. Since the dominant mode in a grasping action is the compressive mode, standard compression tests were considered for the samples. The universal electrodynamic testing machine, ElectroForce 3200 Test Instruments from Bose Inc., was used for these tests. To avoid the complexity of the nonlinear characteristics of elastomeric materials, the load range was confined to the linear range. Each sample was tested twice, so that each material was tested six times. The load (displacement) was applied in a ramp fashion (0.05 mm/sec), and both the deformation and the load were measured and recorded during the test. The nominal stress-strain curves were

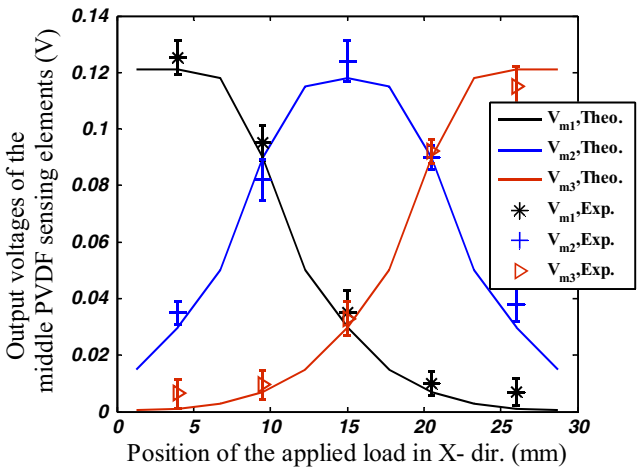

Fig. 28 Output voltages of the middle sensing elements versus the *X*-location of the load

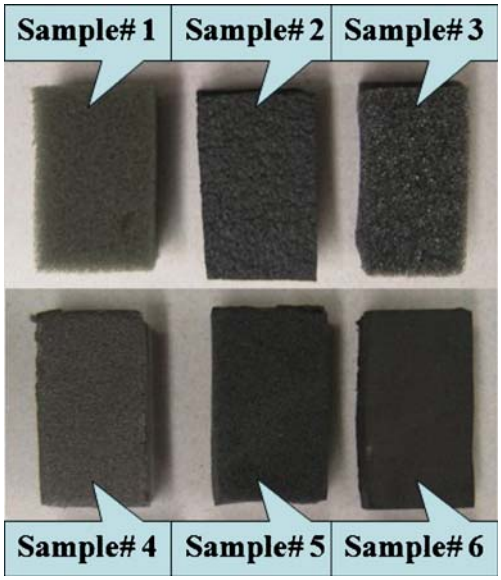

Fig. 29 Elastomers with different softness used in the experiment

calculated using the initial length and the initial area of the samples. A very good consistency among the obtained curves was observed. However, data were averaged point-by-point and an average stress-stain curve was obtained for each sample. The Young's modulus of the elastomers for the linear region were obtained as follows: E_1=0.1 MPa, E_2=0.76 MPa, E_3=3 MPa, E_4=7.4 MPa, E_5=11.15 MPa, and E_6=60 MPa, where E_1 stands for Young's modulus of sample #1, E_2 stands for Young's modulus of sample #2, and so on. These samples are shown in Fig. 29.

After the characterization tests, elastomers were tested using the microfabricated sensors. Figure 30 shows that an elastomeric material is placed on the sensor and a distributed load is applied by the shaker. While a distributed load of 5 N was applied on the top of each elastomer, the

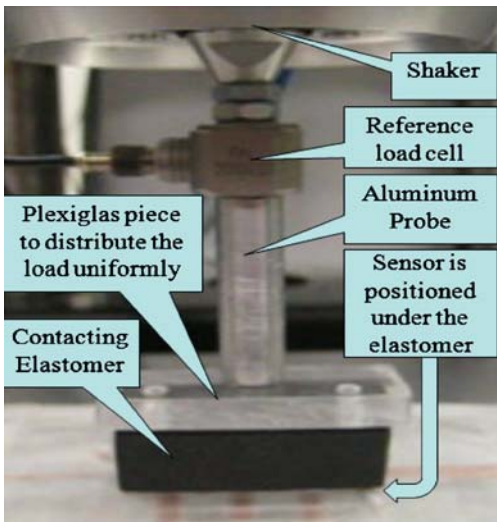

Fig. 30 A uniform distributed load was applied on the top of the elastomers

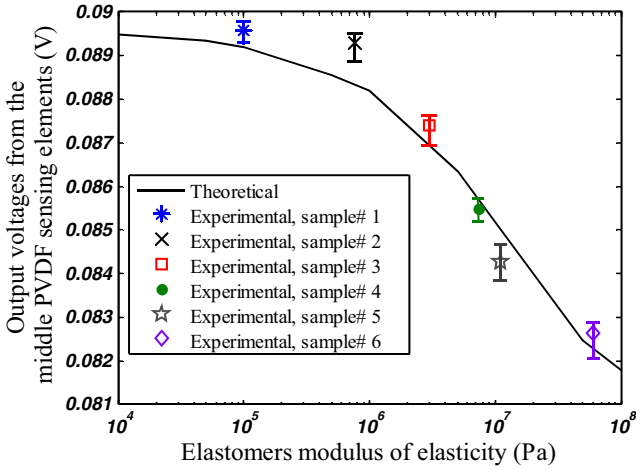

Fig. 31 Output voltages of the middle PVDF sensing elements versus modulus of elasticity of the tested elastomers at 5 N grasping loads

output voltage of the middle PVDF sensing elements was recorded. The output voltages of the middle PVDF sensing elements versus the modulus of elasticity of the contacting elastomers for the 5 N distributed uniform load are shown in Fig. 31.

To investigate the effect of grasping loads on the output of the sensor, three different grasping loads (F_1=1N, F_2=3N, and F_3=5N) were applied. Since the Young's modulus of the elastomers varied slightly in this force range, the associated modulus of elasticity for each elastomer was recalculated for each force, using the stress–strain relationship. Then the output voltages of the sensing elements for each contacting object and for the force magnitude were recorded. The relationship between the middle PVDF output voltage and the modulus of elasticity of the contacting object at different grasping forces are shown in Fig. 32. As shown in Figs. 31, and 32, the experimental and

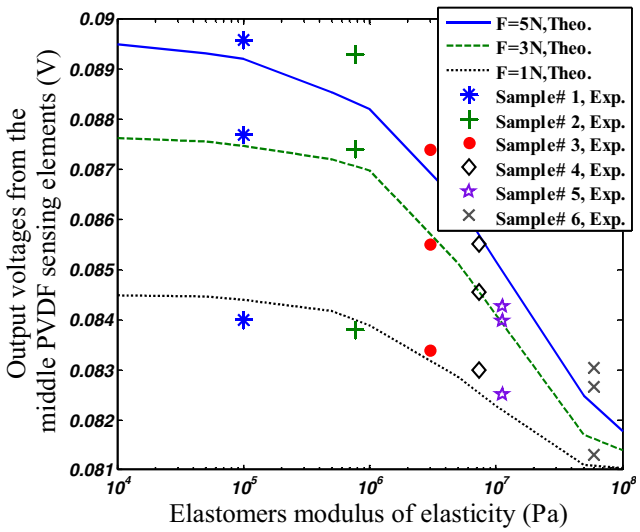

Fig. 32 Output voltages at the middle PVDF sensing elements versus different elastomers at different grasping loads

theoretical results for various applied forces are in close conformity.

As discussed earlier, it is observed that a higher grasping force leads to a smaller deviation between the theoretical and experimental results.

One more factor that affects the accuracy of the theoretical and experimental results is the fact that in the theoretical analysis elastomerics were modeled as linear elastic materials, but in the experiments they exhibit non-linear properties.

6 Summary and conclusion

A MEMS tactile sensor for use in minimally invasive surgery is modeled, characterized, and tested. The sensor is designed to be integrated within existing MIS graspers and is thus able to measure the *in vivo* properties of grasped tissues. Measuring the mechanical properties of soft tissue *in situ* and *in vivo* is important as the *in vivo* and *ex vivo* mechanical properties of tissue are dramatically different. The real time measurement of the tissue properties including the non-linear hyperelastic and viscoelastic behaviors of tissue is beneficial for many branches in this area. The material properties of grasped tissues can be determined at any instant, using the force and displacement data that the sensor reports. In addition, the sensor is capable of finding the position of applied point loads. This capability is essential in the detection and collection of information about hidden anatomical features such as lumps or arteries. The dimensions of the sensor are selected such that it can be integrated with most MIS graspers. In addition, a sensor with these dimensions is, on the one hand, sensitive enough to detect the pulsation of grasped arteries and, on the other hand, strong enough to withstand the grasping loads. The present sensor comprises three sensing units; however, any number of sensing units can be considered. In the experiments, a small cross talk between the three sensing units was observed. This cross talk can be attributed to the part of the load that is carried by the structure and affects the adjacent sensing units. Experiments indicate that the softness sensor is more accurate at higher grasping loads. There are many other issues to be considered in order to commercialize the sensor. In particular, further miniaturization, deposition of PVDF, wiring, packaging, sterilizing, and disposal are some of the challenges to be addressed.

References

F. Beer, E. Johnston, J. DeWolf, *Mechanics of Materials* (McGraw-Hill Higher Education, Boston, 2006)

J. Brown, J. Rosen, M. Sinanan, B. Hannaford, In-vivo and postmortem compressive properties of porcine abdominal organs Lect. Notes Comput. Sci. **2878**, 238–245 (2003)Medical Image Computing and Computer-Assisted Intervention, MICCAI, Toronto, Canada

D. Chong, W. Lee, J. Pang, T. Low, B. Lim, Mechanical Failure Strength Characterization of Silicon Dice, 5th Electronics Packaging Technology Conference, Singapore, 10–12 December, 2003

J. Dargahi, S. Najarian, Human tactile perception as a standard for artificial tactile sensing—a review Int. J. Med. Robot. Comput. Assist. Surg. **1**(1), 23–35 (2004)

J. Dargahi, M. Parameswaran, S.M. Payandeh, A micromachined piezoelectric tactile sensor for an endoscopic grasper:theory, fabrication and experiments J. Microelectromech. Syst. **9**(3), 329–335 (2000) Sep

J. Dargahi, S. Najarian, V. Mirjalili, B. Liu, Modeling and testing of a sensor capable of determining the stiffness of biological tissues Can. J. Electr. Comput. Eng. **32**(2), 45–51 (2007a)

J. Dargahi, S. Najarian, B. Liu, Sensitivity analysis of a novel tactile probe for measurement of tissue softness with applications in biomedical robotics J. Mater. Process. Technol. **183**, 176–182 (2007b)

J. Dargahi, S. Najarian, R. Ramezanifard, F. Ghomshe, Fabrication and testing of a medical surgical instrument capable of detecting simulated embedded lumps Am. J. Appl. Sci. **4**(5), 957–964 (2007c)

G. Emamieh, A. Ameri, S. Najarian, A. Golpaygani, Experimental and theoretical analysis of a novel flexible membrane tactile sensor Am. J. Appl. Sci. **5**(2), 122–128 (2008)

F. Ericson, J. Schweitz, Micromechanical fracture strength of silicon J. Appl. Physi. **68**(11), 5840–5844 (1990)

A. Golpaygani, S. Najarian, G. Emamieh, Design and modeling of a new tactile sensor based on membrane deflection Am. J. Appl. Sci. **4**(10), 813–819 (2007)

A. Golpaygani, S. Najarian, M. Movahedi, G. Emamieh, Fabrication of a capacitance-based tactile sensor with biomedical applications Am. J. Appl. Sci. **5**(2), 129–135 (2008)

M. Hosseini, S. Najarian, S. Motaghinasab, J. Dargahi, Detection of tumors using a computational tactile sensing approach Int. J. Med. Robot. Comput. Assist. Surg. **1**(2), 333–340 (2006)

R. Howe, Y. Matsuoka, Robotics for surgery Annu. Rev. Biomed. Eng. **1**, 211–240 (1999)

R. Howe, W. Peine, D. Kontarinis, J. Son, Remote palpation technology for surgical applications IEEE Eng. Med. Biol. Mag. **14**(3), 318–323 (1995)

T. Ikeda, *Fundamentals of Piezoelectricity* (Oxford Science Publications, New York, NY, 1996)

A.E. Kerdok, S.M. Cotin, M.P. Ottensmeyer, A.M. Galea, R.D. Howe, S.L. Dawson, Truth Cube: Establishing physical standards for soft tissue simulation Med. Image Anal. **7**(3), 283–291 (2003) September

Y. Kurodaa, M. Nakaob, T. Kurodac, H. Oyamad, M. Komorie, Interaction model between elastic objects for haptic feedback considering collisions of soft tissue Comput. Methods Programs Biomed. **80**, 216–224 (2005)

Y.S. Lee, K.D. Wise, A batch-fabricated silicon capacitive pressure transducer with low temperature sensitivity IEEE Trans. Electron Devices **ED-29**, 42–48 (1982)

A. Melzer, G. Buess, A. Cuschieri, *Instruments and Allied Technology for Endoscopic Surgery. Operative Manual of Endoscopic Surgery 2* (Springer-Verlag, New York, 1994), pp. 1–69

F. Nahas, A. Farah, D. Solia, Suspicious node found at the time of reduction mammaplasty Aesthet. Plast. Surg. **26**, 54–56 (2002)

N. Narayanan, A. Bonakdar, J. Dargahi, M. Packirisamy, R. Bhat, Design and analysis of a micromachined piezoelectric sensor for measuring the viscoelastic properties of tissues in minimally invasive surgery J. Smart Mater. Struct. **15**, 1684–1690 (2006)

M. Ottermo, O. Stavdahl, T. Johansen, Palpation Instrument for Augmented Minimally Invasive Surgery, 2004 IEEE/RSJ International Conference on Intelligent Robots and Systems, Japan (2004), September 28

W. Peine, J. Son, R. Howe, A Palpation System for Artery Localization in Laparoscopic Surgery, First International Symposium on Medical Robotics and Computer-Assisted Surgery, Pittsburgh (1994), Sept. 22–24.

K. Petersen, Silicon as a mechanical material. Proc. IEEE **70**(5) (1982), May

M.A. Qasaimeh, I. Stiharu, J. Dargahi, Design and analysis of a micromachined tactile sensor for minimally invasive surgery. International Conference on Dynamics, Instrumentation and Control, Queretaro, Mexico, August 13–16, 2006.

M.A. Qasaimeh, S. Sokhanvar, J. Dargahi, M. Kahrizi, PVDF-based microfabricated tactile sensor for endoscopic minimally invasive surgery. IEEE/ASME Journal of Micro-Electro-Mechanical Systems (2007), to appear

K. Rebello, Applications of MEMS in surgery Proc. IEEE **92**(1), 43–55 (2004)

W.K.D. Samaun, J.B. Angell, An IC piezoresistive pressure sensor for biomedical instrumentation IEEE Trans. Biomed. Eng. **BME-20**, 101–109 (1973)

S. Sokhanvar, M. Packirisamy, J. Dargahi, A multifunctional PVDF-based tactile sensor for minimally invasive surgery J. Smart Mater. Struct. **16**, 989–998 (2007a)

S. Sokhanvar, A. Zabihollah, R. Sedaghati, Investigating the effect of the orthotropic property of piezoelectric PVDF on its sensing and actuating capabilities and response of the system Trans. Can. Soc. Mech. Eng. **31**(1), 111–125 (2007b)

S. Sokhanvar, J. Dargahi, M. Packirisamy, Influence of friction on piezoelectric sensors. Sens. Actuators, A, Phys., **141**, 120–128 (2008), http://dx.doi.org/10.1016/j.sna.2007.07.035

K. Suzuki, K. Najafi, K.D. Wise, A 1024-element high-performance silicon tactile imager IEEE Trans. Electron Devices **37**, 1852–1859 (1990)

H. Tanigawa, T. Ishihara, M. Hirata, K. Suzuki, MOS integrated silicon pressure sensor. IEEE Trans. Electron Devices **ED-32**, 1191–1195 (1985)

V.J. Thomas, K.M. Patil, S. Radhakrishnan, Three-dimensional stress analysis for the mechanics of plantar ulcers in diabetic neuropathy Med. Biol. Eng. Comput. **42**, 230–235 (2004)

P. Ueberschlag, PVDF piezoelectric polymer Sens. Rev. **21**(2), 118–126 (2001)

J.G. Webster, Tactile sensors for robotics and medicine (Wiley-Interscience Publication, New York, 1988)

P.S. Wellman, R.D. Howe, The mechanical properties of breast tissue in compression, Technical Report No. 99003 (Hravard BioRobotics Laboratory, Cambridge, MA, USA, 1999)